ACS APPLIED NANO MATERIALS

www.acsanm.org Article

Ultrafast and Controllable Construction of Sb Particle-Loaded Bead-Like Carbon Nanofibers for Long Cycle-Life Sodium-Ion Storage

Xin Luo, Xueyan Wu,* Yanchun Pei, Yan Lv, Rui Xue, Chunmei Ma, Chan Liu, and Jixi Guo*

Cite This: https://doi.org/10.1021/acsanm.4c06192 Read Online

ACCESS | Metrics & More | Article Recommendations | Supporting Information

ABSTRACT: Antimony (Sb) exhibits excellent conductivity and reactivity with sodium ions, which can be attributed to its distinctive puckered layer structure. Additionally, it has the potential to achieve a high theoretical capacity of 660 mAh g^{-1} through the formation of Na_3Sb. However, the significant volume expansion (approximately 390%) that occurs during the charging process restricts its practical applications. To tackle these challenges, we developed a fast Joule heating technique to successfully ultrafast construct Sb nanoparticles into the bead-like structure of N,S-codoped asphalt-based carbon fibers (N/S-CNF). This unique bead-like structure effectively inhibits the volume expansion of the metal during the charging and discharging process. In addition, the 1D carbon nanofibers contribute to the formation of a robust electrode framework and enable fast electron transfer during cycling to facilitate the kinetics. These advantages together contribute to the excellent cycling stability and rate performance of self-supported Sb@N/S-CNF nanocomposites used as anode materials for sodium-ion batteries (SIBs). The specific capacity was still as high as 263.46 mAh g^{-1} at 0.1 A g^{-1}after 150 cycles and 221.1 mAh g^{-1} at 0.5 A g^{-1} after 750 cycles with a capacity retention rate of 83.9%. These findings provide ideas for the ultrafast preparation of binder-free Na^+ storage nanomaterials.

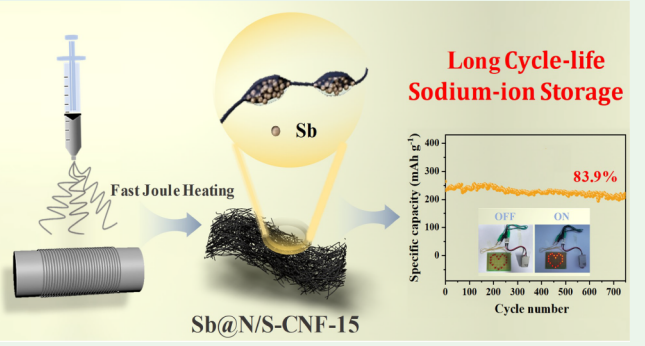

KEYWORDS: *antimony, carbon fiber network, heteroatom doping, sodium-ion battery, full battery*

1. INTRODUCTION

Currently, lithium-ion batteries (LIBs), known for their high energy and functional density, are extensively used in mobile electronics and electric vehicles among high-performance energy storage devices.[1−3] However, with the growth in demand for energy storage and the increasing consumption of lithium resources, it has been widely recognized that there is a shortage of lithium resources and their uneven global distribution.[4] As a consequence, researchers have spent the past decade in search of alternatives to LIBs, including sodium-ion batteries (SIBs), potassium-ion batteries (PIBs), and zinc-ion batteries (ZIBs). Among them, SIBs are deemed to be the most prospective next-generation energy storage technology due to their abundant raw material resources and wide global distribution.[3] However, sodium ions (1.02 Å) have a larger radius compared to lithium ions (0.76 Å), making them harder to insert into the anode material, resulting in a lower reversible capacity.[5] Consequently, developing an anode material with a high theoretical capacity is crucial for enhancing the electrochemical performance of sodium-ion batteries.[6,7]

Sb-based anode materials are notable among potential options due to their high theoretical specific capacity (660 mAh g^{-1}), good safety features, ease of synthesis, and low production costs.[8−12] However, Sb-based materials undergo tremendous volume expansion (390%) during the de-embedding of Na^+, resulting in the breakdown of the working electrode and the possible detachment of the active material from the current collector. These problems ultimately cause a rapid attenuation of high-rate performance and cycling stability.[13−16] In addition, nanomaterials can significantly shorten the diffusion distance of Na^+ to improve reaction kinetics. By controlling the morphology and achieving nanoscale dimensions, more active sites for Na^+ storage are provided in Sb-based materials.[17] Ramireddy et al.[18] evaluated the effect of Sb size and composition in Sb carbon nanocomposites on the electrochemical performance and Na^+ storage mechanism, finding that ultrafine Sb nanocrystals favor the reversible conversion reaction and exhibit the best cycling stability. However, the high specific surface area and oversized antimony-electrolyte interface lead to the formation of an unstable solid electrolyte interface (SEI) and side

Received: November 4, 2024
Revised: February 3, 2025
Accepted: February 6, 2025

reactions during cycling, which are unfavorable for sodium storage performance.

The introduction of carbon materials with well-designed structures can prevent direct contact between the electrolyte and Sb-based electrodes, which helps to build a stable SEI and reduce side reactions.[19] The carbon layer provides a larger buffer space for the Sb-based material to mitigate volume fluctuations, maintaining the structural integrity of the electrode during charge/discharge cycling.[14] Li et al.[20] designed and prepared a sandwich-like carbon-coated Sb/graphene material (G@Sb@C). It demonstrated excellent cycling stability, achieving a reversible capacity of 569.5 mAh g^{-1} after 200 cycles at a current density of 100 mA g^{-1} when used as an anode material for SIBs. Therefore, the construction of Sb/C nanocomposites can keep the stability of the material structure. In contrast to three-dimensional (3D) and two-dimensional (2D) nanomaterials, one-dimensional nanomaterials can effectively reduce the diffusion paths for ions and electrons, resulting in faster diffusion kinetics.[16] Electrospinning is a simple, controllable, and mature technique for the preparation of various one-dimensional cross-linked reticulated carbon composites. Hu et al.[21] prepared 1D composite flexible electrodes of Sb@C by electrospinning, which significantly improves the cycling stability of Sb materials. The previous work in which Sb nanoparticles were uniformly distributed in carbon fibers could not satisfy the multiplicity performance requirement. The bead-like structure in the nanofibers effectively mitigates the volume expansion of Sb during sodium storage, thereby preventing the metal from detaching from the material's surface and facilitating the establishment of fast reaction kinetics through electron transfer channels. Li et al.[22] used N-doped carbon nanofibers radially aligned with MIL-88A and $Ti_3C_2T_x$ MXene nanolaminates by electrospinning, in situ growth, calcination, and freeze-drying methods to synthesize bead-like porous $Ti_3C_2T_x$ MXene-based heterostructure aerogels, which achieved rapid ion/electron diffusion and provided structural durability. However, creating these beaded structures typically involves complex synthesis processes. It is significant to use a simple method to prepare composite nanofibers with the above bead-like structures.

In this article, we designed a 1D N,S-codoped carbon nanofiber coated with Sb nanoparticles (Sb@N/S-CNF) using a straightforward electrospinning method. Sb nanoparticles were rapidly reduced and encapsulated in the bead-like structure of carbon nanofibers, which effectively inhibits the volume expansion of Sb metal during charging and discharging. In addition, the N,S-codoped carbon fiber network structure can enhance electronic conductivity and provide an abundance of active sites and effective transport channels. At the same time, the Sb@N/S-CNF self-supported carbon fiber film eliminates the need for conductive agents and binders, which significantly improves the energy density of the battery. These advantages of the Sb@N/S-CNF composites synergistically lead to notable enhancements in their sodium storage performance. The results showed that the Sb@N/S-CNF anode has good cycling stability and rate performance, with a reversible capacity of 263.4 mAh g^{-1} after 150 cycles at 0.1 A g^{-1} and a high-rate capacity of 221.1 mAh g^{-1} at 0.5 A g^{-1} after 750 cycles.

2. EXPERIMENTAL SECTIONS

2.1. Chemical Material. Pitch was obtained from Karamay, Xinjiang. Polyacrylonitrile (PAN, Mw = 150,000), antimony acetate ($C_6H_9O_6Sb$), thiourea (NH_4N_2S), and N,N-dimethylformamide (DMF, >99.8 wt %) were purchased from Shanghai Aladdin Biochemical Technology Co., Ltd.

2.2. Materials Preparation. For the preparation of the spinning solution, 0.8 g of PAN and 0.8 g of pitch were dissolved in 10 mL of DMF in a 20 mL beaker with vigorous magnetic stirring. The solution was then mixed with 0.8 g of $C_6H_9O_6Sb$ for another 2 h at 80 °C. Following that, 74.5 mg of thiourea was added to the mixture. After 12 h of stirring, a black electrospinning precursor solution was formed. After that, the precursor solution was placed in a syringe. The needle was 20 cm away from the aluminum foil collector, and the voltage was set to 15 kV. The nanofiber film was calcined in a muffle furnace at 300 °C for 2 h at a heating rate of 1 °C min^{-1}. The flexible Sb@N/S-CNF-*xx* (*xx* means the content of Sb) membrane was then obtained by a Joule heating process with the current set to 200 A and the voltage set to 40 V, and rapidly heated up to 900 °C within 1.6 s in an argon atmosphere (plot of discharge time versus temperature in Figure S1). For a typical process, the Sb content in the Sb@N/S-CNF composite was designed at 15 wt %. For comparison, several samples with higher Sb contents (10 and 20 wt %) were synthesized. Sb@CNF and CNF were prepared similarly to Sb@N/S-CNF-15.

2.3. Materials Characterization. The morphological features and distribution of elements in the samples were examined by scanning electron microscopy (SEM, Hitachi S-4800) and transmission electron microscopy (TEM, JEM 2100F (200 kV)) coupled with an energy dispersion spectrometer (EDS). Powder XRD spectra were acquired using a SmartLab SE X-ray diffractometer with filtered Cu Kα radiation (1.54056 Å). Raman spectroscopy was conducted on a Bruker Senterra dispersive Raman microscope at an excitation wavelength of 532 nm. Fourier transform infrared (FTIR) spectra were obtained for all samples utilizing a Bruker VERTEX 70 spectrometer, scanning the range of 400−4000 cm^{-1}. The chemical state of the sample was analyzed using X-ray photoelectron spectroscopy (XPS) with Al−Kα radiation (1486.6 eV), performed on a Thermo Fisher Scientific ESCALAB 250 spectrometer. Thermogravimetric analysis was also conducted using a Hitachi STA3700. The flexible test was conducted using Flex Test Mini−S-P equipment.

2.4. Electrochemical Characterization. The working electrodes were punched into discs with a diameter of 12 mm and were direct binder-free electrodes. Next, the average mass of active material loaded onto the electrodes reached nearly 1.2 mg cm^{-2}. Na metal was used as a counter and reference electrode in the assembled half-cells. Electrochemical properties were evaluated using CR2032-type coin cells with glass fiber (Whatman) as the diaphragm and a 1 M $NaClO_4$ solution mixed with ethylene carbonate (EC) and diethyl carbonate (DEC) (1:1 volumetric ratio). Cyclic voltammetry (CV, 0.01−3 V) tests at different scan rates and electrochemical impedance spectroscopy (EIS) were performed on the CellTest System 1470E (Solartron Analytical) electrochemical workstation. The galvanostatic discharge/charge (GDC) performances of the cells were carried out using the LAND CT2001A.

3. RESULTS AND DISCUSSION

3.1. Morphological and Structural Characterization. The preparation of the self-supported Sb@N/S-CNF electrode is depicted in Figure 1a. First, the spin stock mixture with

https://doi.org/10.1021/acsanm.4c06192
ACS Appl. Nano Mater. XXXX, XXX, XXX−XXX

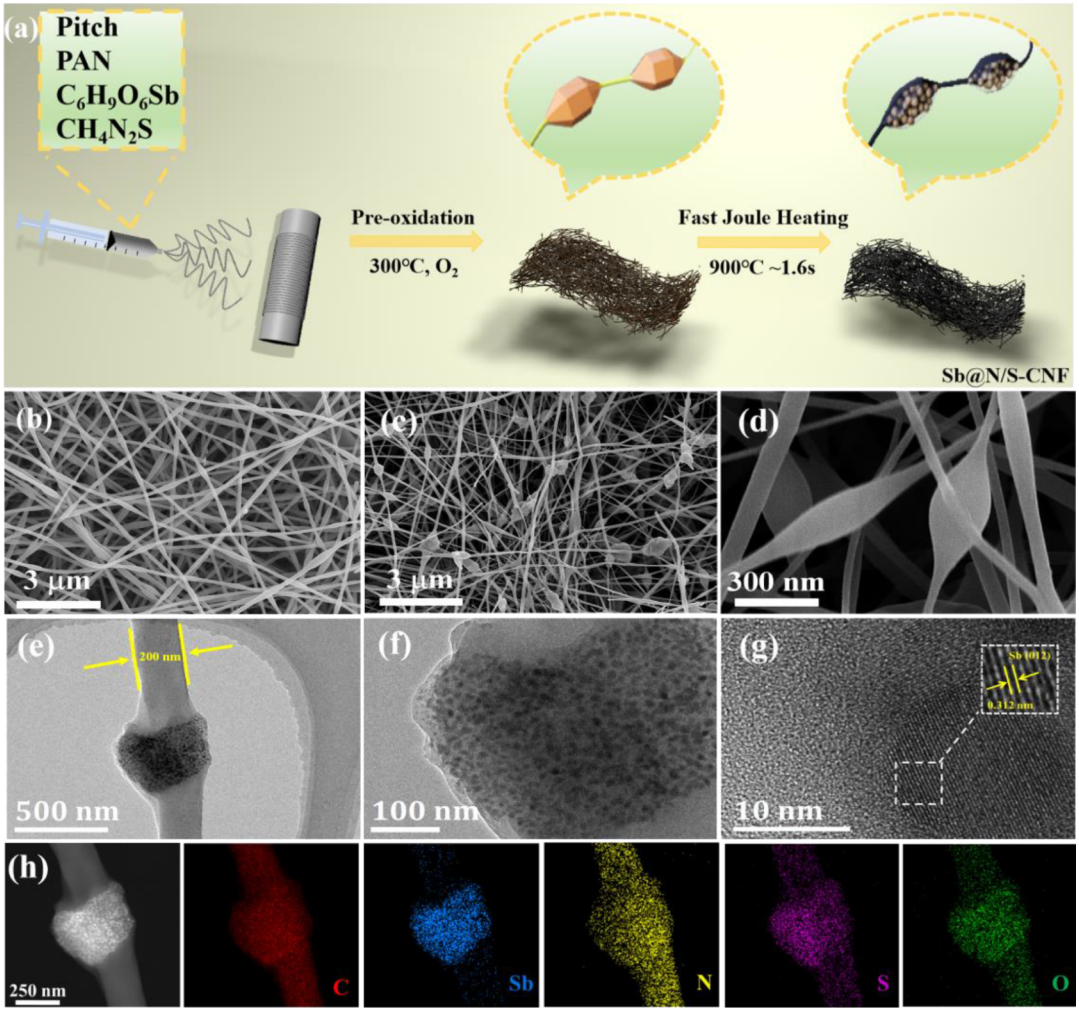

Figure 1. (a) Schematic illustration of the synthetic process. SEM images of (b) CNF, and (c,d) Sb@N/S-CNF-15 composites. (e,f) TEM, (g) HRTEM, and (h) EDS mapping images of Sb@N/S-CNF-15.

DMF, PAN, CH_4N_2S, pitch, and $C_6H_9O_6Sb$ was electrospun to obtain a yellowish-brown fiber film. Then, the black Sb@N/S-CNF material was obtained after 2 h of preoxidation and Joule heating for rapid carbonization. The flexible Sb@N/S-CNF can be used directly in sodium-ion electrodes without conductive agents and binders. After folding and stretching a 1000 times, the original morphology of Sb@N/S-CNF-15 can be recovered without fracture (Figure S2), which proves that the material has good flexibility and can be used as a flexible and self-supporting electrode for direct assembly. During the high-temperature carbonization process, in situ reduction of Sb^{3+} ions to metallic Sb occurs, encapsulated in bead-like structures. Meanwhile, under the same carbonization conditions, the excess carbon origin served as a reductant, which had the capability to completely reduce Sb_2O_4 to Sb. Thus, it can generate the targeted Sb@N/S-CNF composite material. It is worth mentioning that the intermediate generated Sb_2O_4 can be easily reduced to Sb metal by carbon due to its instability.

As depicted in Figure 1b, the one-dimensional (1D) carbon fiber had a randomly oriented nonwoven structure, and its diameter was about 115 nm (Figure S3). Specific surface area, pore volume, and pore size information are given in Table S1 for the three samples. 1D nanofibers have the unique merits of a high specific area and a high surface-to-volume ratio, facilitating the transport of sodium ions and electrons and increasing the area of contact between the electrolyte and the active materials. Compared with CNF, Sb@N/S-CNF-15 has a smaller contact angle between the electrode material and the electrolyte (Figure S4). The good wettability of the composite material facilitates rapid electrolyte penetration, reducing the internal resistance of the battery and improving its charge/discharge rate. Interestingly, with the addition of coal pitch to reduce the PAN concentration, the nanofibers appeared to have spindle knots and a rough film surface, which possessed the characteristics of a large surface area and more defects. The emergence of spindle knots was mainly because the reduction of polymer concentration significantly decreased the viscosity and electrical conductivity of the solution, which facilitated the formation of solid bead-like nanofibers. Lower viscosity and conductivity may result in the collapse of the liquid jet into droplets, thus creating electrospray.[23] The Sb@N/S-CNF also had a unique morphological characteristic of solid bead-like fibers in Figure 1c,d. $C_6H_9O_6Sb$ was thermally decomposed and converted to nanoscale carbon-coated Sb-based metal particles, which were mainly concentrated in spindles with a rough film surface. At the same time, compared with CNF, the fiber morphology of Sb@N/S-CNF had changed greatly, with fibers of different thicknesses and surfaces adhering to each other, creating a three-dimensional dendritic fabric. That was the result of the gradual fusion and adhesion of the fiber

https://doi.org/10.1021/acsanm.4c06192
ACS Appl. Nano Mater. XXXX, XXX, XXX−XXX

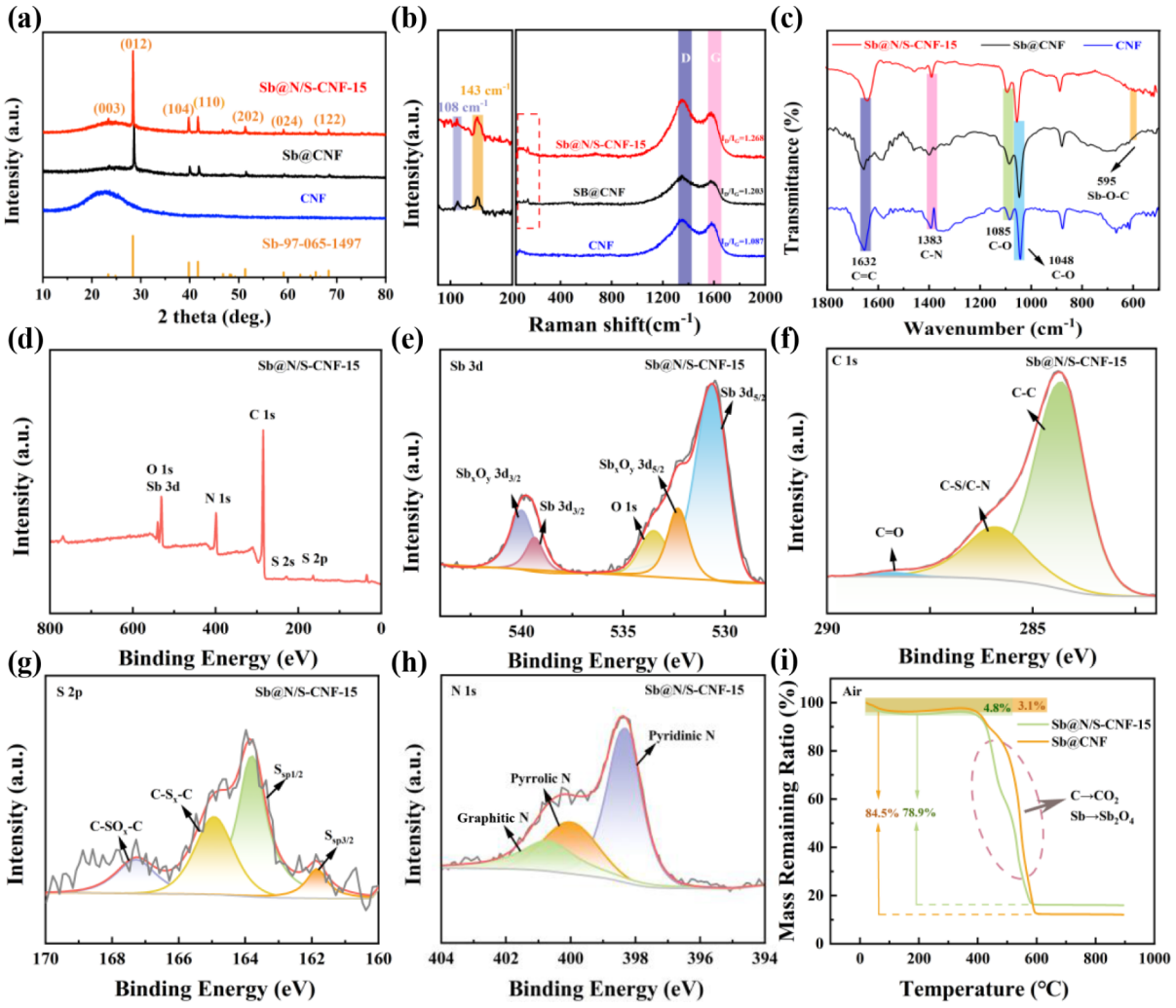

Figure 2. (a) XRD patterns and (b, c) Raman spectrum and FT-IR spectrum of Sb@N/S-CNF-15, Sb@CNF and CNF. (d) XPS spectra of Sb@N/S-CNF-15. (e) Sb 3*d*, (f) C 1*s*, (g) S 2*p*, (h) N 1*s* spectra. (i) TG curves of Sb@N/S-CNF-15 and Sb@CNF.

surfaces during the process of carbonization at elevated temperatures, which was conducive to the improvement of the electrically conductive properties of the carbon fibers. Furthermore, morphologies of Sb@CNF, Sb@N/S-CNF-10. and Sb@N/S-CNF-20 were also characterized, displaying a solid bead-like network structure (Figure S5). As depicted in Figure 1e,f, the Sb-based metal particles were uniformly distributed in the junction, accompanied by a slight agglomeration. The HRTEM image (Figure 1g) illustrates that Sb-based metal particles are wrapped by an amorphous shell layer, and a crystalline distance of 0.312 nm is characteristic of the Sb (012) crystallographic planes (PDF#97-065-1497). As shown in Figure 1h, the elemental mapping revealed that most of the Sb and S elements were tightly distributed in the fiber nodules, which may be the reason for the good stability of flexible electrode materials during charging and discharging. The distribution of N and S elements in the carbon fibers was consistent, with both being uniformly distributed.[24,25] The S element was also uniformly distributed in the fibers and complementary to the N element. Additionally, the introduction of oxygen atoms during the preoxidation process resulted in a uniform distribution of the O element in the fibers.

This uniformity is attributed to the reaction of Sb metal on the fiber surface with oxygen to form Sb_xO_y, consistent with the XPS results (Figure 2d).[26] The combination of Sb metal with asphalt-based carbon fibers greatly improves the electrical conductivity of carbon materials, and the electrical conductivity parameters of each sample were tested (Figure S6 and Table S2). From the calculated results, it is evident that the conductivity decreases with the reduction of the Sb metal content, which is not favorable for the transport of electrolyte ions. Carbon fibers supply ample active sites for Na^+ storage due to their dual doping properties of S and N.

The crystalline phase of Sb@N/S-CNF-15, Sb@CNF, and CNF was characterized through XRD. In Figure 2a, all the derivative peaks of Sb@N/S-CNF-15 were well identifiable as Sb (JCPDS Card No. 97-65-1497) with no impurity peaks, indicating that the element is of high purity. Compared to carbon nanofibers (CNFs), the peaks of amorphous carbon (~24) exhibited broader and flatter features, which were most likely due to the doping of the elements S and N, as well as the compounding of ultrafine Sb nanoparticles, thus inducing a widening of the interlayer spacing. Moreover, the physical phase of Sb@N/S-CNF-10 and Sb@N/S- CNF-20 was also characterized by XRD, as illustrated in Figure S7. The Raman spectra of Sb@N/S-CNF-15, Sb@CNF, and CNF (Figure 2b).

https://doi.org/10.1021/acsanm.4c06192
ACS Appl. Nano Mater. XXXX, XXX, XXX−XXX

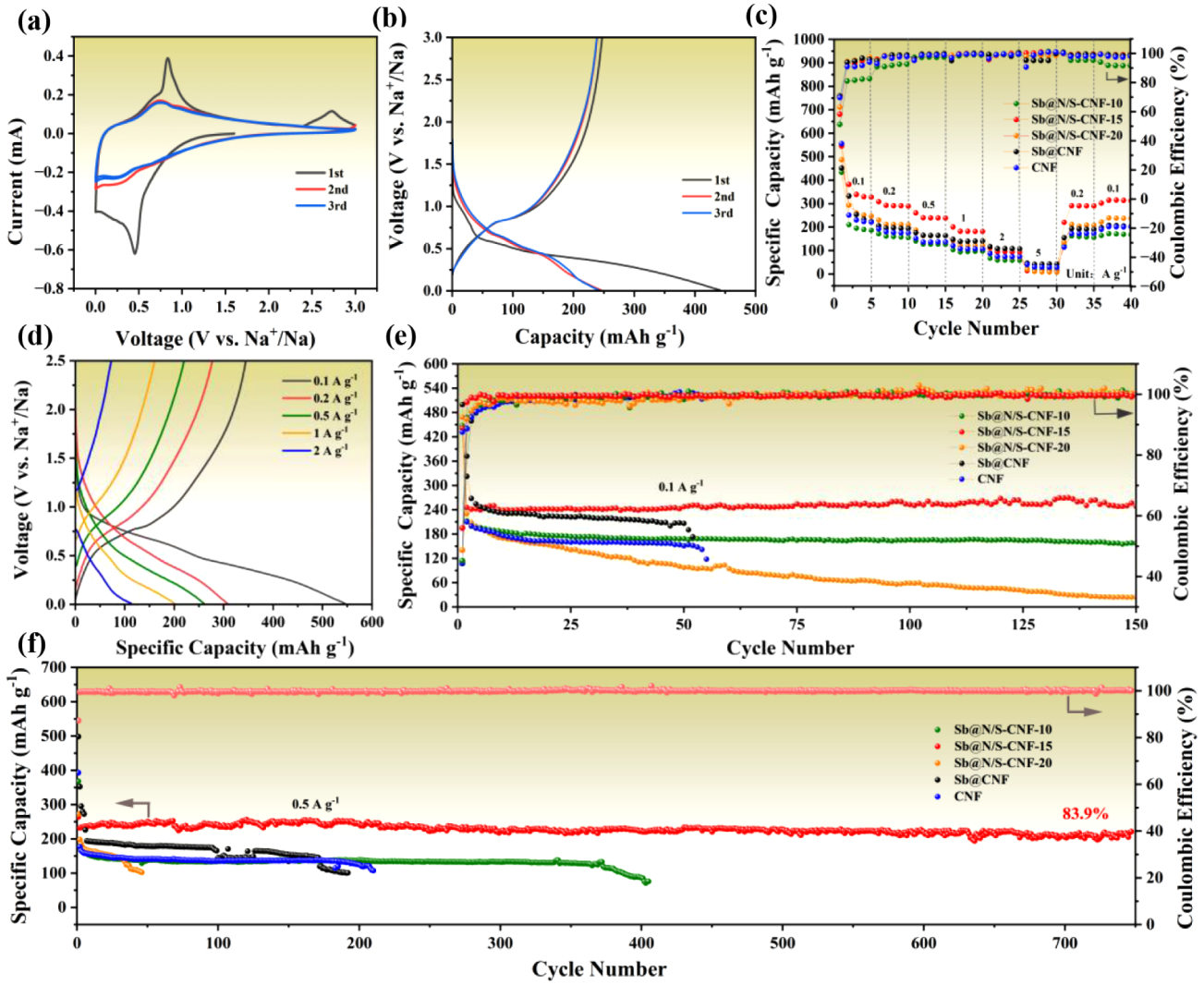

Figure 3. Electrochemical Na storage performances of Sb@N/S-CNF-10, 15, 20, Sb@CNF and CNF. (a) CV curves of Sb@N/S-CNF-15 at a scan rate of 0.1 mV s^{-1} at a potential of 0.01−3.0 V. (b) GDC profiles of Sb@N/S-CNF-15 at a current density of 0.1 A g^{-1}. (c) Rate performance and Coulombic efficiency of Sb@N/S-CNF-10, 15, 20, and Sb@CNF and CNF anodes with current densities ranging from 0.1 to 5.0 A g^{-1}. (d) Charge and discharge profiles at current densities ranging from 0.1 to 5.0 A g^{-1}. (e) Cycling performance and Coulombic efficiency of Sb@N/S-CNF F-10, 15, 20, Sb@CNF and CNF anodes at a current density of 0.1 A g^{-1}. (f) Cycling performance and Coulombic efficiency of Sb@N/S-CNF-10, 15, 20, Sb@CNF and CNF anodes at a current density of 0.5 A g^{-1}.

It is widely recognized that the I_D/I_G ratio can be used to reveal the degree of disorder in graphite. This spectrum proved that the strength ratio of the D to the G band (I_D/I_G) was higher for Sb@N/S-CNF-15, indicating that there existed a number of defects on the carbon interface of Sb@N/S-CNF-15.[27] Moreover, two other peaks located on the spectrum at 108 and 143 cm^{-1} were typically characteristic peaks of Sb, and the result of their Raman was compatible with the result of XRD.[9] The FTIR was investigated for the functional groups of Sb@N/S-CNF-15, Sb@CNF, and CNF electrode materials (Figure 2c). The characterized peak at 1383 cm^{-1} correlated to the C−N stretching vibrational signals,[28] demonstrating the validation of successful N doping in the composites. The characteristic peaks of the C−O stretching vibrations of phenol hydroxyl and hydroxymethyl groups were noticed at 1085 and 1048 cm^{-1}.[29] The characteristic peak near 599 cm^{-1} was traced to Sb−O−C vibrations.[30,31] Due to the robust chemical bonding between the active substance and the carbon-based substrate, the electrochemical activation was enhanced, which in turn boosted the electron/ion mobilization rate. The chemical bonds connect Sb to the carbon fibers, effectively preventing the active materials from detaching and maintaining the structural integrity of the Sb@N/S-CNF-15 and Sb@CNF composites during prolonged cycling. Additionally, these chemical bonds enhance electrochemical activity and promote the rapid transfer of electrons.[32−34]

The XPS (Figure 2d) illuminates the existence of the elements Sb, C, S, N, and O in sample Sb@N/S-CNF-15. In the high-resolution Sb 3*d* spectrum (Figure 2e), the two peaks situated at 530.35 ($3d_{5/2}$) and 538.91 eV ($3d_{3/2}$) can be attributed to the metal state of Sb. The binding energies of 532.06 eV ($3d_{5/2}$) and 539.78 eV ($3d_{3/2}$) are consistent with the oxide binding energies of Sb, which are attributed to the oxidation of some Sb nanoparticles during the preoxidation process, forming Sb_xO_y on the surface of carbon fibers.[26] Given the phenomenon of overlap between the Sb 3d and O 1*s* core peaks, the fraction located at 533.62 eV is reasonably inferred to originate from the contribution of the O 1*s* orbital.[31] For the

https://doi.org/10.1021/acsanm.4c06192
ACS Appl. Nano Mater. XXXX, XXX, XXX−XXX

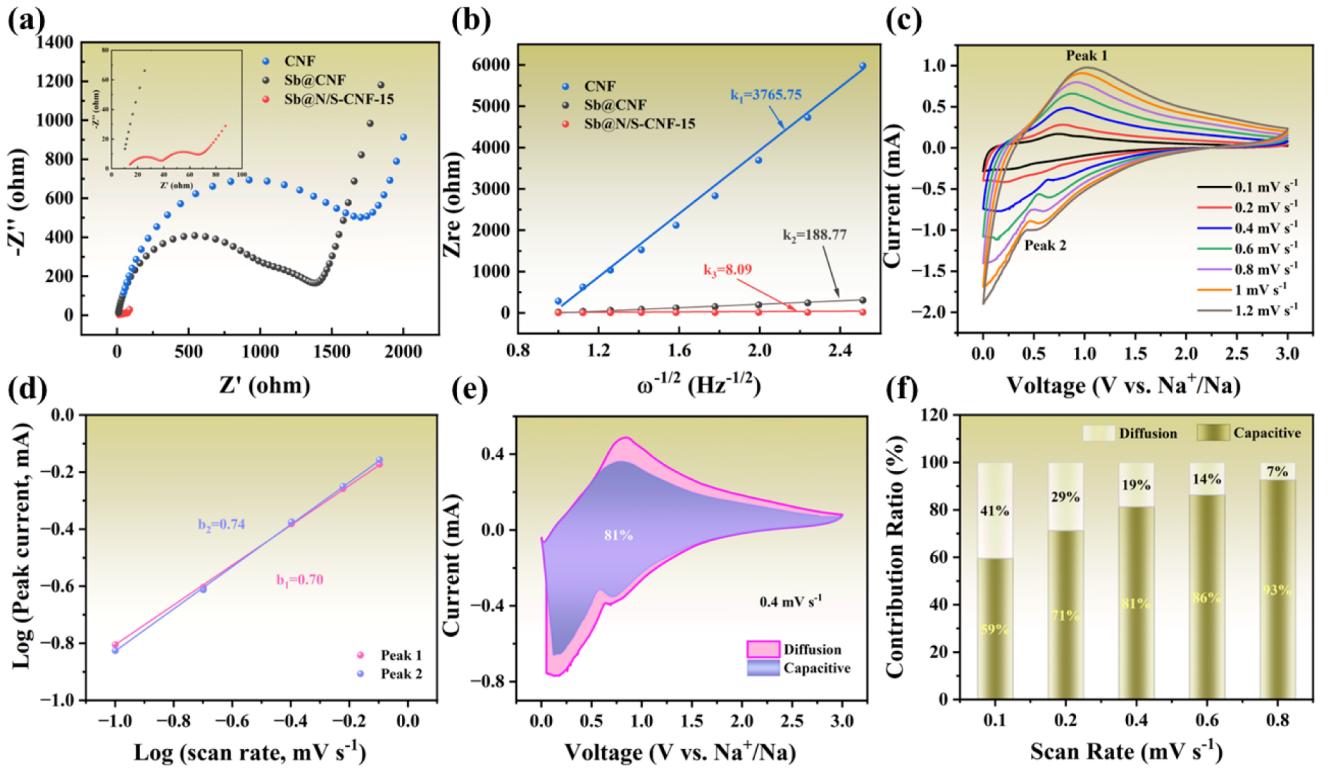

Figure 4. (a)EIS curves of Sb@N/S-CNF, Sb@CNF and CNF anodes. (b) relation between Zre and $\omega^{-1/2}$ in the low-frequency zone. (c) The CV curves of Sb@N/S-CNF-15 electrode at various scan rates from 0.1 to 1.2 mV s^{-1}. (d) The relationship between peak currents and scan rates. (e) Capacitive contribution curves at the scan rate of 0.4 mV s^{-1}. (f) contribution ratio of capacitive-controlled capacities for Sb@N/S-CNF-15 electrode at different scan rates.

C 1*s* of the Sb@N/S-CNF-15 (Figure 2f), three peaks were observed at 284.83, 286.12, and 288.35 eV, corresponding to the C 1*s* in the states of C−C, C−S/C−N, and C═O.[36] As shown in Figure 2g, S 2p peaks for Sb@N/S-CNF-15, S $2p_{3/2}$, S $2p_{1/2}$, C−S_x−C, and C−SO_x−C showed band energies of 161.92, 163.98, 164.98, and 168.58 eV, respectively. The C−SO_x−C bond might be generated in the carbonization procedure.[37] There are three peaks in the N 1*s* spectrum scan (Figure 2h) centered at 398.29, 400.00, and 400.70 eV, which belong to pyridine N, pyrrole N, and graphite N.[38] The doping of heteroatoms (N and S) and the in situ embedding of Sb-based microparticles effectively facilitated the electrolyte percolation process and increased the reaction site of Sb@N/S-CNF-15, improving the electrochemical properties in the Sb@N/S-CNF-15 electrode.[39] The Sb content in Sb@N/S-CNF-15 and Sb@CNF electrodes was then measured by TGA at a ramp rate of 10 °C min^{-1} in an atmosphere of oxygen (Figure 2i). The initial weight reduction in the range of 20−400 °C was caused by the vaporization of adsorbed water. Specifically, the respective weight reductions were 4.8% and 3.1%. The second weight loss around 400−550 °C was primarily due to the complete oxidation of Sb and C to form Sb_2O_4 and CO_2. These weight reductions were measured at 84.5% and 78.9%, respectively. The Sb contents in the Sb@N/S-CNF-15 and Sb@CNF electrodes were 6.4% and 4.9%, respectively, by the following eq 1:[40]

$$\mathrm{Sb(wt.\ \%)} = \frac{2 \times \mathrm{Sb_2O_4(wt.\%)} \times M_{\mathrm{Sb}}}{M_{\mathrm{Sb_2O_4}}} \quad (1)$$

where $M_{\mathrm{Sb_2O_4}}$ and M_{Sb} and Sb (wt. %) and Sb_2O_4 (wt. %) are the weight percent of Sb_2O_4 and Sb, respectively.

3.2. Na^+ Storage Properties in Half Cells. The electrochemical properties of the prepared samples were tested in CR2032 button cells, which were assembled with a sodium foil as a counter electrode. Cyclic voltammetry (CV) curves were first collected at 0.1 mV s^{-1} to investigate the detailed electrochemical reaction process and are shown in Figure 3a. In the initial cycle of cathode scanning, an irreversible Na^+ insertion peak was observed at 0.49 V, which is closely interrelated with the generation of Na_xSb during the preliminary sodiation step and the formation of the solid electrolyte interphase (SEI). During the last two cycles of cathode scanning, two distinct peaks were located at 0.72 V and 0.25 V, which were ascribed to the two-step reaction of Sb, generating the intermediate Na_xSb and the Na_3Sb alloys. The two oxidizing peaks appeared at potentials of 0.73 and 0.89 V, respectively, which were related to the transformation of Na_3Sb to the interposer Na_xSb and its recovery to Sb through the Na^+ deinsertion, respectively.[41,42] The second and third CV scans almost repeat the results, showing that Sb@N/S-CNF-15 had excellent stability and reactivity. The alloying-dealloying reactive steps of Sb@N/S-CNF-15 in the whole reaction process can be depicted as follows:

$$\mathrm{Sb} + x\mathrm{Na^+} + x\mathrm{e^-} \leftrightarrow \mathrm{Na}_x\mathrm{Sb} \quad (2)$$

$$\mathrm{Na}_x\mathrm{Sb} + (3-x)\mathrm{Na^+} + (3-x)\mathrm{e^-} \leftrightarrow \mathrm{Na_3Sb} \quad (3)$$

As shown in Figure S8, the CV curves of Sb@CNF, Sb@N/S-CNF-10, and Sb@N/S-CNF-20 are similar to those of Sb@N/S-CNF-15, exhibiting irreversible Na^+ insertion peaks and

https://doi.org/10.1021/acsanm.4c06192
ACS Appl. Nano Mater. XXXX, XXX, XXX−XXX

two pairs of reversible redox peaks corresponding to the alloying and dealloying of Sb metal. The initial scan of the CNF exhibited a distinct anodic peak signal at 0.53 V, correlating with the formation of the SEI. The absence of significant peaks in the cathodic scans confirmed the difference between CNF and other materials. The CNF electrode does not undergo the alloying of antimony and the subsequent dealloying process.

Figure 3b demonstrates the Sb@N/S-CNF-15 GDC curves with a current density of 0.1 A g^{-1}. During the first cycle, the initial discharge and charge capacities of the material were, respectively, 441.4 mAh g^{-1} and 247.1 mAh g^{-1}, with an initial Coulombic efficiency (ICE) of 55.99%. In comparison to Sb@N/S-CNF-10 (45.18%), Sb@N/S-CNF-20 (48.73%), Sb@CNF (44.58%), and CNF (48.73%), Sb@N/S-CNF-15 has a higher ICE. The unrecovered capacity may be attributed to the formation of an SEI on the electrode surface. The irreversible loss of capacity may result from the formation of the SEI film on the electrode surface as well as the occurrence of side reactions. The result was consistent with the conclusions obtained from the CV tests. The rate properties of Sb@N/S-CNF-15 were evaluated by varying the current densities ranging from 0.1 to 5.0 A g^{-1} in Figure 3c, yielding reversible capacities of 545.4, 307.7, 260.3, 180.7, 90.5, and 13.5 mAh g^{-1} when the current densities were 0.1, 0.2, 0.5, 1.0, 2.0, and 5.0 A g^{-1}, respectively. The capacity of the Sb@N/S-CNF-15 electrode can be returned to 302.2 mAh g^{-1} as the current density goes back to 0.1 A g^{-1}, indicating that it maintains its structural stability over a wide range of current density variations. Notably, CNF can provide only a very low-rate capacity, which shows that the modification of the carbon materials plays a key role in the significant enhancement of the rate capacity. In addition, a straightforward comparison between Sb@N/S-CNF-15 and Sb@CNF demonstrated that the doping of S and N was able to significantly improve the rate properties. Figure 3d depicts the GDC curves of Sb@N/S-CNF-15 at different current densities from 0.1 to 5.0 A g^{-1}, and they illustrate a high degree of reversibility with increasing current density, and its capacity decay phenomenon is negligible. In addition, the electrochemical impedance spectroscopy tests verified this (Figure 4a). As shown in Figure 3e, the cycling performances of Sb@N/S-CNF-10, Sb@N/S-CNF-15, Sb@N/S-CNF-20, Sb@CNF, and CNF at a 0.1 A g^{-1} electrode are illustrated. The anode composed of Sb@N/S-CNF-15 exhibits the highest stability capacity with a high reversible capacity of 263.4 mAh g^{-1} after 150 cycles, and almost 100% Coulombic efficiency was maintained. In contrast, Sb@N/S-CNF-10, Sb@N/S-CNF-20, Sb@CNF, and CNF display lower capacities of 157.5 mAh g^{-1} after 150 cycles, 24.6 mAh g^{-1} after 150 cycles, 206.0 mAh g^{-1} after 50 cycles, and 117.8 mAh g^{-1} after 55 cycles, respectively. Likewise, the Sb@N/S-CNF-15 displays excellent capacity retention compared with other materials in SIBs. To evaluate its long-lasting cycling stability under high-rate conditions, we examined the cycling stability of Sb@N/S-CNF-15 under a high current density of 0.5 A g^{-1} (Figure 3f). Remarkably, the Sb@N/S-CNF-15 electrodes still have outstanding capacity retention and have been cycled up to 750 cycles (221.1 mAh g^{-1}) with 83.9% capacity retention. In addition, to further explore the reason why Sb@N/S-CNF-15 exhibits excellent cycling stability, we disassembled the sodium half-cells that were cycled for 100 cycles at 0.5 A g^{-1} for morphological characterization.

The optical photograph and SEM images of Sb@N/S-CNF-15 after cycling are shown in Figures S9 and S10. The structure of Sb@N/S-CNF-15 after cycling was found to be well-protected, indicating excellent structural stability and effectively buffering the volumetric expansion generated by Sb during cycling. The XRD spectra show that the (012) and (110) crystal planes of Sb correspond to the hexagonal crystal system (PDF #97-065-1497) (Figure S11). This is consistent with the physical phase of Sb before cycling, where Sb maintains the hexagonal crystal system structure. It indicates that the intercalation and expulsion of sodium ions do not lead to the change of crystal structure during the charging and discharging process, which is one of the reasons for the excellent cycling stability of Sb@N/S-CNF-15. The good flexibility of the carbon fibers helps to maintain the structural integrity of the composites, preventing breakage during charging and discharging (Figure S2). The Sb@N/S-CNF-15 electrode material exhibits good reversibility and stability during cycling, which is attributed to the structural stability of the composite materials. Different carbon configurations efficiently buffered the chalking and reunions of Sb nanoparticles, thus conserving their structural stability. The Sb@N/S-CNF-15 in SIBs has such excellent electrochemical properties in the SIBs system, making it one of the more outstanding results among the asphalt-based carbon fiber structures and Sb composites reported in the literature so far (Table S4). Compared with typical Na^+ storage systems, although the Sb@N/S-CNF-15 composite has a low capacity at specific current densities and its cycling performance needs to be improved, due to its unique structurally optimized design, which contains antimony as well as nitrogen- and sulfur-*co*-doped carbon frameworks, it still exhibits excellent cycling performance and capacity performance.

To explore the properties of the reaction kinetics of the CNF, Sb@CNF, and Sb@N/S-CNF-15 electrodes in more depth, we performed an exhaustive analysis using electrochemical impedance spectroscopy (EIS). Figure 4a illustrates Nyquist plots that visually reflect the electrochemical performance of the electrodes. Standard EIS curves tend to contain two prominent regions: the high-frequency region usually exhibits semicircular arc shapes, while the low-frequency region is characterized by a diagonal line. The sloping line in the low-frequency region is generally recognized as the hindering force encountered by Na^+ as it diffuses within the electrode material. In the mid- to high-frequency region, the semicircular arc region usually represents the solid electrolyte interfacial resistance (R_{SEI}) and the charge migration impedance (R_{ct}), which together affect the charge transfer efficiency of the electrodes during charging and discharging. In this equivalent circuit (Figure S12), Relect represents the contact resistance between the electrode and the electrolyte, Q is related to the capacity of the SEI membrane, and C represents the capacity involved in the charge migration process. In particular, W_0 is used to describe the Warburg impedance properties in relation to the diffusion behavior of Na^+.[43−45] Compared to Sb@CNF (419 Ω) and CNF (1514 Ω), Sb@N/S-CNF-15 has the smallest charge resistance (R_{ct}) of 27 Ω (Figure 4a), which suggests that the well-designed Sb@N/S-CNF-15 structure can enhance the electronic conductivity, promote ion diffusion, and accelerate the charge transfer process. In addition, Figure S12 illustrates the larger R_{ct} of Sb@N/S-CNF-10 and Sb@N/S-CNF-20. In an attempt to have a more intuitive understanding of the relationship between the real part impedance

https://doi.org/10.1021/acsanm.4c06192
ACS Appl. Nano Mater. XXXX, XXX, XXX−XXX

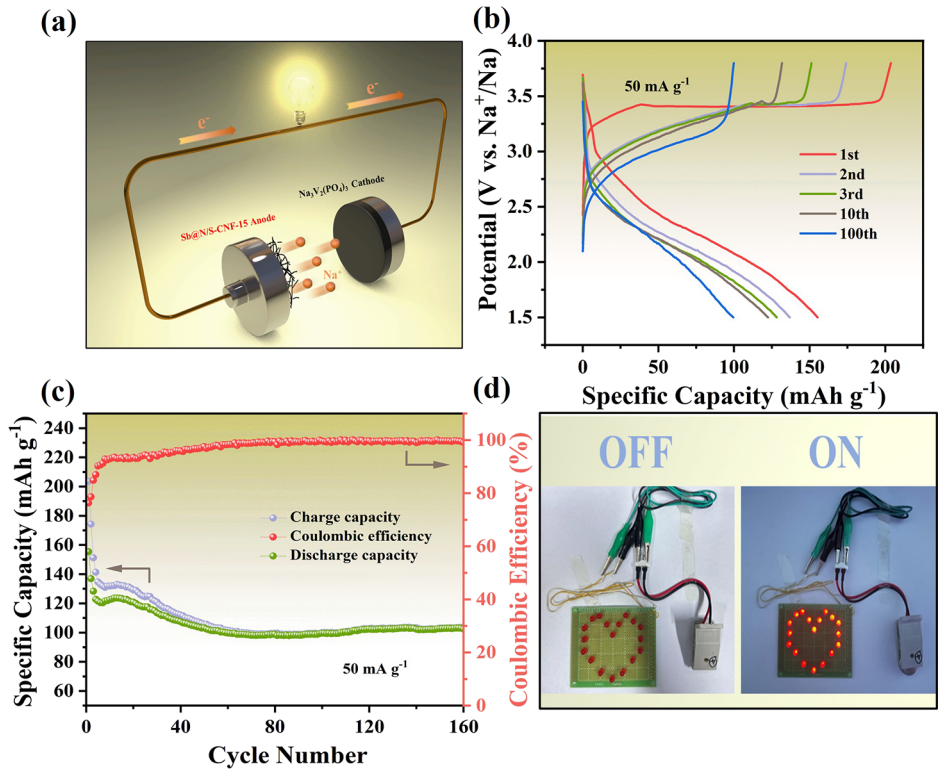

Figure 5. (a) Schematic illustration of full cell fabrication consisting of the Sb@N/S-CNF-15 anode $Na_3V_2(PO_4)_3$ cathode. (b) GCD curves and (c) cycling performance of the Sb@N/S-CNF-15||$Na_3V_2(PO_4)_3$ full cell. (d) Digital photographs of a red LED (2 V) lightened by the Sb@N/S-CNF-15||$Na_3V_2(PO_4)_3$ full cell.

(Z_{re}) and the frequency ($\omega^{-1/2}$), a sloping straight line was fitted and plotted in the frequency interval from 0.1 to 1.0 Hz according to eq 5 as follows:[46]

$$Z_{re} = R_{SEI} + R_{ct} + k\omega^{-1/2} \tag{4}$$

where Z_{re} shows a linear relationship with $\omega^{-1/2}$ and k represents the slope of the fitting line. It is particularly striking that the dispersion coefficient (D_{Na^+}) for sodium ions (Na^+) from the activated substance can be accurately computed by the formula (eq 5).

$$D_{Na^+} = \frac{R^2T^2}{2A^2n^4F^4C^2K^2} \tag{5}$$

In this equation, R is the constant of the gas(8.314 J mol^{-1} K^{-1}), T is the temperature of the room (298 K), A is defined as the electrode's surface area (1.13 cm^2), n is the amount of electrons transferred each particle during a chemical reaction, F is the normal Faraday constant (96,500 C mol^{-1}), C represents the sodium ion concentration (1.0×10^{-3} mol cm^{-3}), and K is the Warburg factor. The value of K can be obtained from the slope of the straight curve in Figure 4b, and the slope value of Sb@N/S-CNF-15 is the smallest at k_3 = 8.09, indicating that the diffusion coefficient of Na^+ in the Sb@N/S-CNF-15 composite is the highest among the samples.[47] The diffusion coefficient D_{Na^+} of Na^+ for the Sb@N/S-CNF-15 composite can be calculated according to eq 4), and the value obtained is 5.22×10^{-12} cm^2 s^{-1}.

To further investigate the reactivity kinetics of the Sb@N/S-CNF-15 anode, the CV was tested at increasing scanning rates varying from 0.1 to 1.2 mV s^{-1} (Figure 4c). It was shown that all the CV curves displayed similar shapes for various scan rates. The relationship between peak current (i) and the scanning rate (ν) is determined by the equation:[48]

$$i = \alpha\nu^b \tag{6}$$

$$\log(i) = b\log(\nu) + \log(\alpha) \tag{7}$$

In this equation, α and b are adjustable factors. It is worth noting that the function of b can be obtained through the ratio between $\log(i)$ and $\log(\nu)$, and the value of b is between 0.5 and 1. According to the calculated b-value, we can infer the Na^+ storage mechanism: a b-value of 0.5 represents a diffusion-controlled mechanism, whereas a b-value of 1.0 implies a surface-controlled pseudocapacitive procedures.[49] In the 0.1–1.2 mV s^{-1} scan rate range, the b-values (Figure 4d) for Peaks 1 and 2 reach about 0.70 and 0.74, revealing the simultaneous contribution of diffusion-controlled mechanisms and surface-controlled pseudocapacitive processes. The capacitance effect ($k_1\nu$) and the ion dispersion procedure ($k_2\nu_{1/2}$) contribution to the current can be calculated by the following equations, while keeping the scan rate constant:[50]

$$i(V) = k_1\nu + k_2\nu_{1/2} \tag{8}$$

Where $i(V)$ signifies the strength of the current in the presence of a continuous voltage, k_1 and k_2 are constants, and $k_1\nu$ is the capacitive contribution to the current. Thus, the capacitive contribution to capacity can be separated from the gross capacity by evaluating the value of k_1. As shown in Figure 4d, at a scan rate of 0.4 mV s^{-1}, the shaded part corresponds to the surface-controlled pseudocapacitive behavior, which contributed 81% to the total capacity. As the scan rate increases, the contribution ratio of the surface-controlled pseudocapacitive behavior gradually increases (Figure 4e). At a

https://doi.org/10.1021/acsanm.4c06192
ACS Appl. Nano Mater. XXXX, XXX, XXX−XXX

scan rate of 0.8 mV s^{-1}, it reaches a high value of 93%. Moreover, the proportion of capacitive effects gradually increases from 59%, 71%, 81%, 86%, and 93% as the scanning speed is accelerated from 0.1, 0.2, 0.4, 0.6, and 0.8 mV s^{-1} (Figure 4f). Sb@N/S-CNF-15 capacitance contributing is significantly higher than that of CNF (Figure S13). This trend showed that the Na^+ storage capacity in Sb@N/S-CNF-15 was mainly affected by the surface-controlled pseudocapacitive behavior. This significant capacitance contribution can be due to the collaborative enhancement effect of Sb and N,S-codoped networks of carbon fibers. The rough surface morphology, wide range of contact interfaces, and excellent electrical conductivity of these networks combine to promote rapid charge accumulation and release, thus giving the material an outstanding rate performance.

To deeply explore the potential of the prepared anode for practical use, we constructed a full cell with a $Na_3V_2(PO_4)_3$ cathode and Sb@N/S-CNF-15 as the anode. The demonstration of its operation mechanism is shown in Figure 5a, where Na^+ ions are delicately embedded and detached between the anodes during the charge−discharge cycle of the cell. Figure 5b presents the charge−discharge curves of the Sb@N/S-CNF-15||$Na_3V_2(PO_4)_3$(NVP) full cell under the potential window of 1.5−3.8 V. The initial discharge capacity of Sb@N/S-CNF-15||NVP reached 155 mAh g^{-1} (as shown in Figure 5b) and displayed excellent cycling stability in terms of cell performance, which was maintained at 103 mAh g^{-1} after 160 cycles at 0.05 A g^{-1} current density (Figure 5c). The properties are superior or comparable to the values in previously reported SIBs, such as $Na(Ni_{1/3}Fe_{1/3}Mn_{1/3})O_2$||Sb@P−N/C,[35] Na@Gra-GC-$MoSe_2$||NVP,[51] NVP||P-ONH-1200,[52] Na-$(Ni_{1/3}Fe_{1/3}Mn_{1/3})O_2$||Sb@P−N/C,[22] and $Na_3V_2(PO_4)_2O_2F$||Sb@N,S-CNFs.[14] Moreover, the Sb@N/S-CNF-15||NVP full cell successfully powered the light emission of a 2 V heart-shaped red LED bulb (shown in Figure 5d). These experimental results undoubtedly support the practicality and effectiveness of Sb@N/S-CNF-15 in sodium-ion battery storage applications.

4. CONCLUSIONS

In summary, one-dimensional beaded Sb@N/S-CNF nanofibers were successfully fabricated by doping the spinning liquid with different doses of antimony source, adopting a fast Joule heating technique. Compared with conventional high-temperature furnace carbonization, this method can complete the carbonization process in just 1.6 s, significantly reducing energy consumption and production time. Self-supported Sb@N/S-CNF electrodes exhibit excellent cycling stability and rate performance. At a current density, the specific capacity reached 263.4 mAh g^{-1} after 150 cycles. Following this, it was noted to remain at 221.1 mAh g^{-1} following 750 cycles of charging and discharging with a current density of 0.5 A g^{-1}, indicating a retained capacitance of 83.9%. Additionally, the full cell assembled with the Sb@N/S-CNF-15 anode and $Na_3V_2(PO_4)_3$ cathode provides a reversible specific capacity of 103 mAh g^{-1} after 160 cycles at 0.05 A g^{-1} current density. The excellent cycling stability is attributed to the following reasons. First, the ultrasmall Sb nanoparticles and high specific surface area nanofibers increase the contact area with the electrolyte and shorten the ion diffusion distance. Second, the beaded carbon skeleton serves as a robust defense against Sb volume changes and maintains its structural integrity during the cycling process, promoting electrolyte diffusion. Third, the codoping of N and S in Sb@N/S-CNF nanocomposites not only improves the electrical conductivity of the composites but also increases the number of active reaction sites. The current research work not only successfully prepared novel antimony-based anode materials but also provided new insights and methodologies for the study of SIBs.

■ ASSOCIATED CONTENT

Supporting Information

The Supporting Information is available free of charge at https://pubs.acs.org/doi/10.1021/acsanm.4c06192.

Additional SEM, optical photo, and XRD analysis data; electrochemical performance (PDF)

■ AUTHOR INFORMATION

Corresponding Authors

Xueyan Wu − *State Key Laboratory of Chemistry and Utilization of Carbon Based Energy Resources, College of Chemistry, Xinjiang University, Urumqi, Xinjiang 830046, PR China*; Email: Wuxy90@xju.edu.cn

Jixi Guo − *State Key Laboratory of Chemistry and Utilization of Carbon Based Energy Resources, College of Chemistry, Xinjiang University, Urumqi, Xinjiang 830046, PR China*; orcid.org/0000-0002-7526-3695; Email: jxguo1012@163.com

Authors

Xin Luo − *State Key Laboratory of Chemistry and Utilization of Carbon Based Energy Resources, College of Chemistry, Xinjiang University, Urumqi, Xinjiang 830046, PR China*

Yanchun Pei − *State Key Laboratory of Chemistry and Utilization of Carbon Based Energy Resources, College of Chemistry, Xinjiang University, Urumqi, Xinjiang 830046, PR China*

Yan Lv − *State Key Laboratory of Chemistry and Utilization of Carbon Based Energy Resources, College of Chemistry, Xinjiang University, Urumqi, Xinjiang 830046, PR China*

Rui Xue − *State Key Laboratory of Chemistry and Utilization of Carbon Based Energy Resources, College of Chemistry, Xinjiang University, Urumqi, Xinjiang 830046, PR China*; orcid.org/0000-0002-0695-0678

Chunmei Ma − *Xinjiang Xuandong Energy Co., Ltd., Hami, Xinjiang 963000, China*

Chan Liu − *State Key Laboratory of Chemistry and Utilization of Carbon Based Energy Resources, College of Chemistry, Xinjiang University, Urumqi, Xinjiang 830046, PR China*

Complete contact information is available at: https://pubs.acs.org/10.1021/acsanm.4c06192

Notes

The authors declare no competing financial interest.

■ ACKNOWLEDGMENTS

This work is supported by the Open Project of the Key Laboratory in the Xinjiang Uygur Autonomous Region of China (2023D04032), the National Natural Science Foundation of China (U2003307, 22105163), the Science and Technology Innovation Leader of the Xinjiang Uygur Autonomous Region of China (2022TSYCLJ0043), the Natural Science Foundation of the Xinjiang Uygur Autonomous Region of China (2021D01D09), and the Hami oil-rich

coal clean and efficient use innovation team (2024hmkjcxtd01).

REFERENCES

(1) Nasajpour-Esfahani, N.; Garmestani, H.; Bagheritabar, M.; Jasim, D. J.; Toghraie, D.; Dadkhah, S.; Firoozeh, H. Comprehensive review of lithium-ion battery materials and development challenges. *Renewable Sustainable Energy Rev.* **2024**, *203*, 114783.
(2) Kim, T.; Song, W.; Son, D.-Y.; Ono, L. K.; Qi, Y. Lithium-ion batteries: Outlook on present, future, and hybridized technologies. *J. Mater. Chem. A* **2019**, *7* (7), 2942−2964.
(3) Zhang, G. X.; Zhu, J. G.; Dai, H. F.; Wei, X. Z. Multi-level intelligence empowering lithium-ion batteries. *J. Energy Chem.* **2024**, *97*, 535−552.
(4) Zhang, C.; Chou, S.; Guo, Z.; Dou, S.-X. Beyond lithium-ion batteries. *Adv. Funct. Mater.* **2024**, *34* (5), 2308001.
(5) Hong, Z.; Maleki, H.; Ludwig, T.; Zhen, Y.; Wilhelm, M.; Lee, D.; Kim, K.-H.; Mathur, S. New insights into carbon-based and MXene anodes for Na and K-ion storage: a review. *J. Energy Chem.* **2021**, *62*, 660−691.
(6) Lai, Q.; Mu, J.; Liu, Z.; Zhao, L.; Gao, X.; Yang, D.; Chen, H.; Luo, W. Tunnel-tType $Na_2Ti_6O_{13}$@Carbon nanowires as anode materials for low-temperature sodium-ion batteries. *Batteries Supercaps* **2023**, *6*, 202200549.
(7) Wu, H.; Xiong, Z. N.; Mao, Y. Y.; Zhang, H. H.; Hu, Y. Y.; Shen, J.; Wang, B. F.; Yu, X. B. MoS_2/MoO_2 nanosheets anchored on carbon cloth for high-performance magnesium- and sodium-ion storage. *J. Mater. Sci. Technol.* **2023**, *143*, 43−53.
(8) Liang, S.; Cheng, Y.-J.; Wang, X.; Xu, Z.; Ma, L.; Xu, H.; Ji, Q.; Zuo, X.; Peter, M.-B.; Xia, Y. G. Impact of CO_2 activation on the structure, composition, and performance of Sb/C nanohybrid lithium/sodium-ion battery anodes. *Nanoscale Adv.* **2021**, *3* (7), 1942−1953.
(9) Han, J. S.; Liu, D. M.; Liu, S. Y.; Shao, W. L.; Yang, E.; Zhang, T. P.; Jin, X.; Jian, X. G.; Hu, F. Y. A collaborative strategy for encapsulating Sb nanoparticles into porous carbon toward high and stable sodium storage. *J. Alloys Compd.* **2022**, *921*, 166054.
(10) Guo, S. T.; Li, H.; Lu, Y.; Liu, Z. F.; Hu, X. L. Lattice softening enables highly reversible sodium storage in anti-pulverization Bi-Sb alloy/carbon nanofibers. *Energy Storage Mater.* **2020**, *27*, 270−278.
(11) Zhang, M.; Ouyang, L. Z.; Zhu, M.; Fang, F.; Liu, J. W.; Liu, Z. W. A phosphorus and carbon composite containing nanocrystalline Sb as a stable and high-capacity anode for sodium ion batteries. *J. Mater. Chem. A* **2020**, *8*, 443−452.
(12) Ge, X. F.; Liu, S. H.; Qiao, M.; Du, Y. C.; Li, Y. F.; Bao, J. C.; Zhou, X. S. Enabling superior electrochemical properties for highly efficient potassium storage by impregnating ultrafine Sb nanocrystals within nanochannel-Containing carbon nanofibers. *Angew. Chem., Int. Ed.* **2019**, *58*, 14578−14583.
(13) Shi, L.; Wang, W. H. Synthesis and sodium storage performance of Sb porous nanostructure. *J. Alloys Compd* **2020**, *846*, 156369.
(14) Qiu, Y.; Fu, F.; Hu, M.; Shen, P. K.; Zhu, J. Tailored chemically bonded metal phosphide@carbon nanowire arrays on foam metal as an all-in-one anode for ultrahigh-Area-capacity sodium-ion batteries. *Chem. Eng. J.* **2023**, *454*, 140402−140402.
(15) Li, X. Y.; Sun, M. L.; Ni, J. F.; Li, L. Template-free construction of self-supported Sb prisms with stable sodium storage. *Adv. Energy Mater.* **2019**, *9*, 1901096.
(16) Fu, F.; Hu, M.; Key, J.; Shen, P. K.; Zhu, J. Carbon encapsulated FeS nanosheet-nanoribbon interwoven sandwich structure as efficient sodium-ion battery anodes. *Carbon* **2023**, *215*, 118469−118469.
(17) Liu, C.; Zeng, F. X.; Xu, L.; Liu, S. Y.; Liu, J. C.; Ai, X. P.; Yang, H. X.; Cao, Y. L. Enhanced cycling stability of antimony anode by downsizing particle and combining carbon nanotube for high-performance sodium-ion batteries. *J. Mater. Sci. Technol.* **2020**, *55*, 81−88.
(18) Ramireddy, T.; Sharma, N.; Xing, T.; Chen, Y.; Leforestier, J.; Glushenkov, A. M. Size and composition effects in Sb-carbon nanocomposites for Sodium-ion batteries. *ACS Appl. Mater. Interfaces* **2016**, *8* (44), 30152−30164.
(19) Chen, H.; Mu, J.-J.; Bian, Y.-H.; Gao, X.-W.; Wang, D.; Liu, Z.-M.; Luo, W.-B. A bimetallic sulfide Co_9S_8/MoS_2/C heterojunction in a three-dimensional carbon structure for increasing sodium ion storage. *New Carbon Mater.* **2023**, *38*, 510−519.
(20) Li, Q. H.; Zhang, W.; Peng, J.; Zhang, W.; Liang, Z. X.; Wu, J. W.; Feng, J. J.; Li, H. X.; Huang, S. M. Metal-organic framework derived ultrafine Sb@Porous carbon octahedron via in situ substitution for high-performance sodium-ion batteries. *ACS Nano* **2021**, *15*, 15104.
(21) Zhu, Y.; Han, X.; Xu, Y.; Liu, Y.; Zheng, S.; Xu, K.; Hu, L.; Wang, C. Electrospun Sb/C fibers for a stable and fast sodium-ion battery anode. *ACS Nano* **2013**, *7*, 6378−6386.
(22) Li, Z.; Long, Z.; Dai, H.; Yan, Z.; Liu, K.; Qiao, H.; Wang, K.; Li, W. Ti_3C_2Tx MXene@Metal-Organic frameworks-derived bead-like carbon nanofibers heterostructure aerogel for enhanced performance lithium/sodium storage. *J. Power Sources* **2024**, *606*, 234586.
(23) Zhang, J.; Ge, J.; Ding, B.; Zhang, F.; Yu, J.; Liu, L. Taro leaf-inspired and superwettable nanonet-covered nanofibrous membranes for high-efficiency oil purification. *Nanoscale Horiz.* **2019**, *4* (5), 1174−1184.
(24) Liu, D. Y.; Yang, L.; Chen, Z. Y.; Zou, G. Q.; Hou, H. S.; Hu, J. G.; Ji, X. B. Ultra-stable Sb confined into N-doped carbon fibers anodes for high-performance potassium-ion batteries. *Sci. Bull.* **2020**, *65*, 1003−1012.
(25) Zhan, W. W.; Zhu, M.; Lan, J. L.; Wang, H. J.; Yuan, H. C.; Yang, X. P.; Sui, G. 1D Sb_2S_3@nitrogen-doped carbon coaxial nanotubes uniformly encapsulated within 3D porous graphene aerogel for fast and stable sodium storage. *Chem. Eng. J.* **2021**, *408*, 128007.
(26) Nguyen, A.-G.; Le, H. T. T.; Verma, R.; Vu, D.-L.; Park, C.-J. Boosting sodium-ion battery performance using an antimony nanoparticle self-embedded in a 3D nitrogen-doped carbon framework anode. *Chem. Eng. J.* **2022**, *429*, 132359−132359.
(27) Jorio, A. H.; Ferreira, E. H. M.; Moutinho, M. V. O.; Stavale, F. A.; Achete, C. A.; Capaz, R. B. Measuring disorder in graphene with the G and D bands. *Phys. Status Solidi B* **2010**, *247* (11−12), 2980−2982.
(28) Xu, M.; Zhang, Y.; Yin, H.; Wang, J.; Li, A.; Corvini, P. F.-X. Efficient catalytic ozonation over Co-ZFO@Mn-CN for oxalic acid degradation: Synergistic effect of oxygen vacancies and HOO-Mn-N_X bonds. *Appl. Catal., B* **2023**, *322*, 122085.
(29) Liu, S. H.; Ban, J. J.; Shi, H. S.; Wu, Z. H.; Shao, G. S.; Cao, G. Q.; Hu, J. H. Near solution-level conductivity of polyvinyl alcohol based electrolyte and the application for fully compliant Al-air battery. *Chem. Eng. J.* **2022**, *431*, 134283.
(30) Xu, A. D.; Huang, C. Y.; Li, G. L.; Zou, K. X.; Sun, H.; Fu, L. L.; Ju, J. H.; Song, Y.; Wu, S. P.; Xu, Z. G.; Yan, Y. R. Sb_2O_3@Sb nanoparticles impregnated in N-doped carbon microcages for ultralong life and high-rate sodium ion batteries. *J. Mater. Chem. A* **2021**, *9*, 12169.
(31) Liu, Y.; Qing, Y.; Zhou, B.; Wang, L.; Pu, B.; Zhou, X.; Wang, Y.; Zhang, M.; Bai, J.; Tang, Q.; Yang, W. Yolk-shell Sb@Void@Graphdiyne Nanoboxes for high-rate and long Cycle life sodium-ion batteries. *ACS Nano* **2023**, *17* (3), 2431−2439.
(32) Wang, S.; Xiong, P.; Guo, X.; Zhang, J. Q.; Gao, X.; Zhang, F.; Tang, X.; Notten, P. H. L.; Wang, G. X. A Stable conversion and alloying anode for potassium-ion batteries: A combined strategy of encapsulation and confinement. *Adv. Funct. Mater.* **2020**, *30* (27), 2001588.
(33) Nunes, N.; Rosa, G. P.; Ferraz, S.; Barreto, M. C.; De Carvalho, M. A. A. P. Fatty acid composition, TLC screening, ATR-FTIR analysis, anti-cholinesterase activity, and in vitro cytotoxicity to A549 tumor cell line of extracts of 3 macroalgae collected in Madeira. *J. Appl. Phycol.* **2020**, *32* (2), 759−771.
(34) Li, H.; Qian, K.; Qin, X.; Liu, D.; Shi, R.; Ran, A.; Han, C.; He, Y.; Kang, F.; Li, B. The different Li/Na ion storage mechanisms of

https://doi.org/10.1021/acsanm.4c06192
ACS Appl. Nano Mater. XXXX, XXX, XXX−XXX

nano Sb_2O_3 anchored on graphene. *J. Power Sources* **2018**, *285*, 114−121.
(35) Zhang, N.; Chen, X.; Xu, J.; He, P.; Ding, X. Hexagonal Sb nanocrystals as high-capacity and long-cycle anode materials for sodium-ion batteries. *ACS Appl. Mater. Interfaces* **2023**, *15* (22), 26728−26736.
(36) Zheng, Y.; Ruan, Q.; Ren, J.; Guo, X.; Zhou, Y.; Zhou, B.; Xu, Q.; Fu, Q.; Wang, S.; Huang, Y. Plasma- assisted liquid-based growth of g-C_3N_4/Mn_2O_3 p-n heterojunction with tunable valence band for photoelectrochemical application Appl. *Catal. B-Environ.* **2023**, *323*, 122170.
(37) Shao, Z. Y.; Meng, H. H.; Sun, J.; Guo, N. K.; Xue, H.; Huang, K. K.; He, F.; Li, F. Y.; Wang, Q. Engineering of amorphous structures and sulfur defects into ultrathin FeS nanosheets to achieve superior electrocatalytic alkaline oxygen evolution. *ACS Appl. Mater. Interfaces* **2020**, *12* (46), 51846−51853.
(38) Zhang, J.; Bai, Q.; Bi, X.; Zhang, C.; Shi, M.; Yu, W. W.; Du, F.; Wang, L.; Wang, Z.; Zhu, Z.; Sui, N. Piezoelectric enhanced peroxidase-like activity of metal-free sulfur doped graphdiyne nanosheets for efficient water pollutant degradation and bacterial disinfection. *Nano Today.* **2022**, *43*, 101429.
(39) Hu, M.; Key, J.; Zhu, M.; He, H.; Wang, N.; Zhu, Y.; Shen, P. K.; Zhu, J. Two-dimensional nanosheet arrays with chemically bonded Cu_2S@NSC heterostructure for efficient sodium-ion storage. *J. Energy Storage.* **2024**, *85*, 111140.
(40) Jing, W. T.; Zhang, T.; Gu, Y.; Zhu, Y. F.; Yang, C. C.; Jiang, Q. N-doped carbon nanonecklaces with encapsulated Sb as a sodium-ion battery anode. *Matter* **2019**, *1*, 720−733.
(41) Wang, X. X.; Feng, B.; Huang, L. M.; Fu, Q. F.; Li, W. Z.; Zhu, C.; Chen, P.; Yang, C. L.; Ding, Y. L. Superior electrochemical performance of Sb-Bi alloy for sodium storage: Understanding from alloying element effects and new cause of capacity attenuation. *J. Power Sources* **2022**, *520*, 230826.
(42) Liu, W. L.; Du, L. Y.; Ju, S. L.; Cheng, X. Y.; Wu, Q.; Hu, Z.; Yu, X. B. Encapsulation of red phosphorus in carbon nanocages with ultrahigh content for high-capacity and long cycle life sodium-ion batteries. *ACS Nano* **2021**, *15*, 5679−5688.
(43) Fan, X. Y.; Jiang, Z.; Huang, L.; Wang, X.; Han, J.; Sun, R.; Gou, L.; Li, D. L.; Ding, Y. L. 3D porous self-standing Sb foam anode with a conformal indium layer for enhanced sodium storage. *ACS Appl. Mater. Interfaces* **2020**, *12*, 20344−20353.
(44) Wei, Q.; Chang, X.; Butts, D.; DeBlock, R.; Lan, K.; Li, J.; Chao, D.; Peng, D.-L.; Dunn, B. Surface-redox sodium-ion storage in anatase titanium oxide. *Nat. Commun.* **2023**, *14* (1), 7.
(45) Butts, D.; Schoiber, J.; Choi, C.; Redhammer, G. J.; Hüsing, N.; Donne, S.; Dunn, B. Fe-substituted sodium β''-Al_2O_3 as a high-rate Na-Ion electrode. *Chem. Mater.* **2021**, *33*, 6136−6145.
(46) Xu, A.; Huang, M.; Liu, C.; Li, T.; Li, X.; Wu, S.; Xu, Z.; Yan, Y. Constructing High-Content Sb Atomic Clusters and Robust Sb—O—C Bond in Sb/C Composites for Ultrahigh Rate and Long-Term Sodium Storage. *Adv. Funct. Mater.* **2024**, *34* (33), 2400302.
(47) Verdianto, A.; Lim, H.; Kang, J. G.; Kim, S.-O. Scalable, colloidal synthesis of SnSb nanoalloy-decorated mesoporous 3D NiO microspheres as a sodium-ion battery anode. *Int. J. Energy Res.* **2021**, *46*, 4267−4278.
(48) Wang, J. W.; Yang, X. F.; Yang, C. N.; Dai, Y.; Chen, S. Y.; Sun, X.; Huang, C. G.; Wu, Y. P.; Situ, Y.; Huang, H. Three-dimensional (3D) ordered macroporous bimetallic (Mn, Fe) selenide/carbon composite with heterojunction interface for high-performance sodium ion batteries. *ACS Appl. Mater. Interfaces* **2023**, *15*, 40100.
(49) Liu, M. M.; Chen, Q. W.; Cao, X. Y.; Tan, D. X.; Ma, J. Z.; Zhang, J. T. Physicochemical confinement effect enables high-performing zinc-iodine batteries J. *Am. Chem. Soc.* **2022**, *144*, 21683−21691.
(50) Wu, Y. J.; Zheng, J. F.; Tong, Y.; Liu, X.; Sun, Y. J.; Niu, L.; Li, H. Y. Carbon hollow tube-confined Sb/Sb_2S_3 nanorod fragments as highly stable anodes for potassium-ion batteries. *ACS Appl. Mater. Interfaces* **2021**, *13*, 51066.
(51) Cao, W.; Liu, M.; Song, W.; Li, Z.; Li, B.; Wang, P.; Fisher, A.; Niu, J.; Wang, F. Regulating sodium deposition behavior by a triple-gradient framework for high-performance sodium metal batteries. *Adv. Sci.* **2024**, *11*, 31.
(52) Wu, W.; Wang, A.; Xu, D.; Huang, C.; Liu, X.; Hu, Z.; Luo, J. A soft carbon material with engineered composition and microstructure for sodium battery anodes. *Nano Energy* **2024**, *128*, 109880.

https://doi.org/10.1021/acsanm.4c06192
ACS Appl. Nano Mater. XXXX, XXX, XXX−XXX